HHS Public Access

Author manuscript

J Appl Phys. Author manuscript; available in PMC 2015 December 03.

Published in final edited form as:

J Appl Phys. 2013 ; 2013: . doi:10.1063/1.4812491.

The effect of ultrafast laser wavelength on ablation properties and implications on sample introduction in inductively coupled plasma mass spectrometry

N. L. LaHaye[1], **S. S. Harilal**[1], **P. K. Diwakar**[1], **A. Hassanein**[1], and **P. Kulkarni**[2]

[1]Center for Materials under Extreme Environment, School of Nuclear Engineering Purdue University, West Lafayette, Indiana 47907, USA

[2]Centers for Disease Control and Prevention, National Institute of Occupational Safety and Health, Cincinnati, Ohio 45213, USA

Abstract

We investigated the role of femtosecond (fs) laser wavelength on laser ablation (LA) and its relation to laser generated aerosol counts and particle distribution, inductively coupled plasma-mass spectrometry (ICP-MS) signal intensity, detection limits, and elemental fractionation. Four different NIST standard reference materials (610, 613, 615, and 616) were ablated using 400 nm and 800 nm fs laser pulses to study the effect of wavelength on laser ablation rate, accuracy, precision, and fractionation. Our results show that the detection limits are lower for 400 nm laser excitation than 800 nm laser excitation at lower laser energies but approximately equal at higher energies. Ablation threshold was also found to be lower for 400 nm than 800 nm laser excitation. Particle size distributions are very similar for 400 nm and 800 nm wavelengths; however, they differ significantly in counts at similar laser fluence levels. This study concludes that 400 nm LA is more beneficial for sample introduction in ICP-MS, particularly when lower laser energies are to be used for ablation.

I. INTRODUCTION

Laser ablation (LA) is a well-known material removal method with application in a variety of fields: analytical chemistry in the form of laser induced breakdown spectroscopy (LIBS) or laser ablation-inductively coupled plasma-mass spectrometry (LA-ICP-MS), thin film fabrication, micromachining, etc.[1–3] LA sample introduction to the ICP allows direct analysis of solid samples with little to no sample preparation.[4] In addition, LA-ICP-MS causes negligible sample destruction, which is useful in applications where little sample is available or minimal damage is desired, and can also provide information about the elemental changes throughout a sample by the use of raster patterns.[4] LA-ICP-MS is a useful analysis technique in geology, archaeology, pharmaceuticals, radioactive waste analysis, and material dating, to name a few.[5–10] One of the main problems facing the accuracy of LA-ICP-MS is elemental fractionation or non-stoichiometric ablation of the sample. Elemental fractionation is influenced by many different parameters, including the element being detected or sample composition,[11] ablation crater aspect ratio (depth to width), laser beam properties, transport of the aerosol from ablation chamber to the ICP, and the ICP itself.[8] Ar and He gases are typically used to flush the aerosol from the ablation

chamber to the ICP-MS.[11] Each gas has its own advantages and minimizes certain fractionation effects in ns-LA. Ar forms more homogeneous aerosols[5] and is more capable of carrying medium and large particles[12] due to its heavier mass, introducing a more representative aerosol into the torch. In a He environment, plasma will expand to farther distances[13] because the lower mass of the ambient gas applies less pressure to the expanding plume than heavier Ar assuming the same gas pressure. This causes less surface re-deposition,[13] and more aerosol is swept from the chamber. He as carrier gas also decreases signal spikes;[12,14] its high thermal conductivity removes energy from the aerosol particles, so particle velocity will be more uniform.

The amount of aerosol introduced to the ICP system also influences fractionation effects that are directly related to laser ablation rate. The ablation rate will depend on laser irradiance; as a crater forms, the irradiance (and subsequently, the laser ablation rate) will decrease due to increased surface area exposed to the laser beam. Craters from single-spot ns-LA are cone-shaped, and increased aspect ratio of these craters indicates a change from photothermal to plasma-dominated ablation, increasing the degree of elemental fractionation.[15] Laser wavelength plays an important role in ns-LA;[16–21] shorter wavelength produces higher mass ablation rate and lower fractionation.[8] This is due to reduced plasma shielding and enhanced laser-target coupling at shorter wavelengths caused by higher critical density of the plasma. Therefore, shorter wavelengths are preferable in ns-LA for the introduction of a more representative and greater quantity of aerosol into the ICP-MS, which in turn will lower fractionation effects.

One factor that greatly affects elemental fractionation is pulse duration. Shorter pulse widths reduce fractionation effects, as shorter pulses create smaller particles[22–24] and also cause fewer thermal effects because the short time scale of the laser pulse does not cause any significant heating of the sample.[25] In fs-LA, plasma will form after the end of the laser pulse, and the laser pulse is shorter than the electron relaxation time, so no thermal effects are observed. In contrast, in ns-LA, the leading edge of the laser pulse will form the plasma and the latter part of the pulse will serve to heat the plasma. The long time scale of ns-LA causes sample melting and mixing, as well as surface redeposition.[4,26]

In this paper, we studied the effects of laser wavelength (400 nm vs. 800 nm) and energy on particle size distribution of aerosol from ablation, signal intensity, and elemental fractionation in fs-LA-ICP-MS of NIST glass standard reference materials (SRMs). Though the influence of laser wavelength on elemental fractionation is well studied in ns-LA-ICP-MS and provides reduced fractionation when the wavelength becomes shorter,[27] the role of fs wavelength on elemental fractionation is not well understood. In fact, it is a controversial subject and fs wavelengths are thought to have little influence in laser ablation[28,29] due to significantly shorter duration of the laser pulse (t_p) compared to electron to ion energy transfer time (τ_{ei}) and heat conduction time (t_{heat}) ($\tau_{ei} \sim t_{heat} \gg t_p$). However, our results show that the fs wavelengths affect the ablation threshold, the ICP-MS signal intensity, detection limits at lower laser energy levels, particle counts, and elemental fractionation.

II. EXPERIMENTAL DETAILS

The experimental configuration of the laser system, beam delivery, and analyzer is shown in the schematic in Figure 1. The laser used is a chirped pulse amplification-based Ti:Sapphire femtosecond laser system (pulse duration 40 fs, Amplitude Technologies), with a wavelength of 800 nm and repetition rate of 10 Hz. Energy of the laser pulses was attenuated using a combination of half-wave plate and thin film polarizer positioned before the compressor optics. The laser wavelength was converted to the second harmonic using a beta barium borate (BBO) crystal (thickness 0.1 mm, group-velocity dispersion (GVD) 20 fs), yielding a wavelength of 400 nm. A dichroic mirror was used to separate 400 nm from residual 800 nm. Temporal broadening occurs due to the objective lens used for focusing, causing the pulse duration at the sample to be approximately 75 fs for both wavelengths. Laser energy stability was less than 2% throughout the experiment.

The laser pulses were transported to the ablation chamber (J100 Series, Applied Spectra) using a series of high reflecting mirrors, and an objective lens focused the laser down to a 100 μm spot size. Visualization of the sample and laser focus was achieved by mounting a CCD camera above the ablation chamber. The ablation chamber was mounted on an XYZ translation stage, allowing for full manipulation of sample position. Sampling time was set to 60 s, resulting in 600 laser pulses forming a single crater. Single spot sampling was used to avoid surface effects and increased transient relative standard deviation (TRSD) introduced by sample rastering.[30] However, crater formation affects ablation rate and can introduce elemental fractionation; this effect may be negligible for fs-LA, but can have a profound effect in ns-LA. Four NIST standards were analyzed (610, 613, 615, and 616) and the following isotopes were detected: Fe-56, Cu-63, Cu-65, Sr-88, Pb-208, Th-232, U-235, and U-238 (concentrations given in Table I). Each analysis started with 10 s of blank, meaning the laser was not triggered until 10 s after the start of data acquisition, then the laser was triggered for 60 s, followed by 40 s of washout time. Ar was used as the carrier gas and was set to a flow rate of 1 l/min.

The aerosol was then analyzed using a quadrupole-based ICP-MS (ICP-MS 7700x, Agilent Technologies Inc.), operated at a power of 1550 W and without use of a collision cell. The first few seconds of signal were ignored to avoid changes in signal associated with surface effects and surface contamination in the introduced aerosol. Data processing was performed by integrating 30 s of signal at the beginning of data acquisition after the initial signal that was ignored.

Particle size distribution of aerosol from ablation was obtained using a scanning mobility particle sizer (TSI Inc., Shoreview, MN), consisting of a differential mobility analyzer (DMA; TSI 3080) and a condensation particle counter (CPC; TSI 3022 A). The sheath flow in the DMA was set to 10 l/min and the aerosol flow was set to 1 l/min. The particle sizer measures mobility size distribution of nanoparticles and submicrometer aerosol using electrical techniques.[31] In addition to particle size distribution measurement, the DMA was also used as a size classifier or a band-pass size filter to sample near-monodisperse particles from the ablation aerosol. Used in this mode, the DMA allowed investigation of ICP-MS signal as a function of one particle size at a time. At this sheath flow, the DMA was able to

classify monodisperse particles with diameters up to 317 nm. Total particle counts were also obtained using the CPC alone. NIST SRM 610 was used as an ablation target to obtain particle size data.

III. RESULTS

The purpose of this work was to obtain information about the role of fs laser wavelength on LA and its relation to laser generated aerosol counts and particle distribution, ICP-MS signal intensity, detection limits, and elemental fractionation. Because the time scale of ablation is shorter than the electron-ion relaxation time, fs wavelength is thought to not have an effect on LA aerosol generation. This work was designed to explore that hypothesis. Several aspects were investigated in order to get a better understanding of the effect of laser wavelength on ablation mechanisms.

A. Wavelength effect on ICP-MS signal

For studying the role of fs laser wavelength on LA, ICP-MS signal for several elements was monitored as a function of laser energy for both 800 nm and 400 nm wavelengths. Eight different isotopes were detected (Fe-56, Cu-63, Cu-65, Sr-88, Pb-208, Th-232, U-235, and U-238); the sum signal (total counts from all the isotopes detected) vs. time is shown in Figure 2 for different laser energies. At all energies, a sharp increase is seen immediately after laser triggering and attains peak signal counts followed by a slow decrease in signal, the slope of which is found to be energy dependent. The difference in signal slope with varying laser energies is due to changes in crater depth as well as crater aspect ratio; both are strongly dependent on irradiation fluence. The signals exhibit near-ablation threshold behaviors at low energies for both wavelengths (~50 μJ at 400 nm and ~150 μJ at 800 nm). Typically, the ablation threshold corresponds to the minimum laser energy or fluence required to remove material from the target of interest. However, at ablation threshold, the ICP-MS may not register a signal due to losses in particle transport; therefore, we define the energy at which the ICP-MS begins to register a signal as near-ablation threshold. The ICP-MS signal at this low laser energy rises very rapidly, then starts to decay after a few seconds; at higher energies, however, the signal maintains approximately the same value for approximately 20 s, with a decrease afterward to one-half to one-third the original value as opposed to decreasing to background level at near-threshold energies. Above threshold, the 400 nm signal shows less of a decrease from peak signal than the 800 nm signal. Figure 3 shows the TRSD for both wavelengths, calculated from the standard deviation of the total signal over a 5 s time period shortly after laser triggering. At 400 nm wavelengths and energies above 200 μJ, the TRSD was consistently 1%–3%. However, the TRSD was higher for 800 nm wavelength at energies below 400 μJ. Higher laser energies also result in a steadier signal with fewer spikes, allowing for more accurate measurements of isotope abundance.

The integral total signal (sum of all eight isotopes detected) was determined by integrating 30 s of the transient signal from the beginning of detection, avoiding the first few seconds to exclude inaccuracies introduced by the initial signal. The results are shown in Figure 4. In both cases, the signal increases linearly with respect to laser energy and a saturation tendency is evident at higher energies. The ICP-MS signal appears to saturate at higher

energy levels; this is more noticeable for 400 nm. It is also clear from the figure that 400 nm laser excitation consistently provided higher signal intensity in the range of laser energy studied compared to 800 nm LA.

B. Wavelength effect on detection capability

The average signals from all four NIST SRM samples (610, 613, 615, and 616) studied were used to create calibration curves to determine the detection limits of the system for various elements and the concentration of unknown samples at various laser energy levels. Four of these calibration curves are shown in Figure 5 and the detection limits are summarized in Table II. The calibration curves were created by ablating the four NIST samples, each with a different concentration of each element investigated, and plotting the certified concentration against the ICP-MS signal intensity. The lowest detectable concentration of trace elements can also be found from the calibration curves. This is computed as

$$detection\ limit = 3 * \sigma_{\mathrm{b}}/\mathrm{s}, \quad (1)$$

where σ_b is the standard deviation of the background signal for the element in question and *s* is the slope of the calibration curve. Some error is introduced here due to extrapolation of the calibration curves to elemental concentrations an order of magnitude below the lowest concentrations of the samples; this error is especially pronounced in Fe and Pb. One important thing to consider is that the more mass ablated, the lower the attainable detection limit, indicating that the best results will be obtained at high energies. As is seen in Table II, detection limits are lower for higher mass elements, namely thorium and uranium, due to their lower background signal. There is less interference at these higher masses than that for lower-massed elements. Detection limits are also lower for 400 nm LA than 800 nm LA at lower energies, but at the highest energies used they approach the same value. This indicates that lower laser energy can be used for 400 nm LA and still yield the same results, which is useful when using a laser with limited energy capabilities. Lower laser energy will also reduce crater effects, which in turn limits elemental fractionation.

C. Elemental fractionation

One measure of elemental fractionation is elemental ratios and how they change as a function of a given parameter. U/Th and U/Pb ratios are a measure of laser- and transport-induced fractionation effects[28] and therefore were examined here. U and Th have approximately identical ionization energies, so ICP conditions should not affect the U/Th ratio; fractionation in the ICP is investigated through the U/Pb ratio.[28] Figures 6 and 7 show the U/Th ratio and U/Pb ratio as a function of wavelength, laser energy, and time. As can be seen in Figure 6, at higher energies, the 400 nm and 800 nm results match closely, both to each other and to the expected values (1.009 ± 0.005 for U/Th and 1.083 ± 0.005 for U/Pb). The results for U/Th are closer to the expected value than U/Pb. However, at lower energies, the 800 nm LA results deviate from both the expected ratio significantly. This could be due to the threshold effect. Figure 7 shows that the TRSD is larger for 800 nm in both ratios and the ratio also increases with time, indicating that fractionation effects are larger for 800 nm LA than for 400 nm LA. The conclusion can be made from this data that the shorter wavelength 400 nm LA results in elemental ratios that more closely match each other, with

less variation, across a wider range of energies, from near-threshold to where the ICP signal is saturated.

D. Particle analysis

Wavelength dependence of particle size distribution was studied in order to gain more insight about changes in ICP-MS signal intensity and elemental fractionation with respect to 400 nm and 800 nm fs-LA sample introduction. A DMA with capabilities to separate out particles with sizes 50–317 nm was connected to a CPC to get relative intensity of the different particle sizes. By performing a scan of the particle diameter, a particle size distribution can be obtained. Typical particle size distribution is shown in Figure 8 for both 400 nm and 800 nm laser excitations obtained with 300/J laser energy. Across all energies used in this study, the most probable diameter falls in the range of 100 nm to 200 nm, with a peak around ~ 100–120 nm. Our results also indicated that the laser energy affects particle size distribution as well as number density. The estimated particle counts for different energy levels of 400 nm and 800 nm excitations is given in Figure 9, as well as the ICP-MS signal intensity from Figure 4 for comparison. Figure 9 shows that the total number of particles increases rapidly with respect to laser energy and saturate at higher energies. Peak particle counts and ICP-MS signal intensity follow the same general trend, especially the results for 400 nm LA. The particle counts are much higher for 400 nm LA than for 800 nm LA, emphasizing the fact that more aerosol is being introduced to the ICP-MS from 400 nm LA than 800 nm LA at the same laser energy. We also noticed the peak aerosol size distribution increased from ~90 nm to ~150 nm when the laser energy is increased from 150 μJ to 500 μJ. Hence, higher laser energies result in a shift in the average aerosol diameter to the higher side, indicating that lower energies should be used to create smaller particle sizes, which will allow for more ionization of the particle within the ICP torch.

We monitored the ICP-MS signal levels for different particle sizes. For this purpose, the DMA was connected before the ICP-MS to act as a band-pass filter, allowing only a narrow range of particle sizes to enter the ICP torch. The changes in ICP-MS signal intensity for various particle sizes are given in Figure 10 for 400 nm and 800 nm LA. The maximum signal is observed for particle sizes 125 nm to 150 nm, with steady signal for particle sizes larger than this. Wavelength does not appear to have an effect in relative contribution of particle sizes, as the trend observed in Figure 10 is the same for both 400 nm and 800 nm wavelengths, even though ICP-MS signals are consistently higher for 400 nm than 800 nm.

We also examined the role of particle size on elemental fractionation. For this, the changes in U/Th and U/Pb elemental ratios were plotted for different particle sizes and are given in Figure 11. As can be seen in Figure 11, little to no particle size dependence is observed for the U/Th ratio for either wavelength, with 400 nm LA giving results closest to the expected ratio of 1.009. Conversely, the U/Pb ratio shows a very large dependence on particle size, with a linear increase for particles with diameter 50 nm to 150 nm and a constant result for particles larger than 150 nm. This shows that particle size will have a large effect on the overall U/Pb ratio observed when not using a particle size filter, so that proper energy and wavelength must be used for LA to yield accurate ratio results. For both ratios, however,

laser wavelength does not seem to have much of an effect on the elemental ratios or elemental fractionation as a function of particle diameter.

IV. DISCUSSION

Our results clearly show that the wavelength of fs-LA influences ICP-MS signal levels, detection limits at lower energies, ablation threshold, and particle counts. The data indicate that fs wavelength plays a crucial role in dictating LA properties. Jiang and Tsai[29] have emphasized that wavelength effects on threshold fluence have yet to be fully characterized and much remains to be explained. In addition, incubation effects can vary as a function of wavelength due to the transparency of the medium to the laser wavelength, but the role of incubation on threshold fluence is also not well-understood.[29] This indicates that in order to fully understand the role of wavelength in LA, we must first gain a better understanding of the underlying ablation mechanisms. Experiments and calculations performed by Stuart *et al.*[32] show that the damage fluence for fused silica is approximately twice as large for 1053 nm LA as opposed to 526 nm LA for pulse widths 0.1 to 10 ps. Therefore, it can be concluded that for comparisons between IR and visible wavelengths, as investigated in this study, wavelength does have an effect on ablation threshold; however, this study only investigated ablation threshold, not the effect on ICP-MS signal results.[32] A previous study showing comparisons between 200 nm and 265 nm fs-LA-ICP-MS results (150 fs FWHM) show that Cu/Zn, U/Th, and U/Pb ratios are very similar for both wavelengths. The fractionation indices also match well for 200 nm and 265 nm fs-LA.[28] However, the similar results could be due to both wavelengths being in the UV range, while our work investigated a comparison between wavelengths in the visible and IR range.

Our present results highlight the various advantages of 400 nm LA over the fundamental wavelength of Ti-Sapphire fs laser. Improved detection limits are evident in signal strength at comparable energy levels; 400 nm LA consistently yields higher signal, as seen in Figure 3. In addition, the shorter wavelength allows for lower laser energy at low detection levels, while 800 nm LA requires higher energies to achieve the same detection limit, as seen in Table II. Based on Figure 3, the 400 nm signal is between 1.2 and 1.4 times greater the 800 nm signal for energies ≤400 μJ. However, this is not consistent with the particle counts seen in Figure 9. It should be remembered that the major mechanism for aerosol formation in laser ablation plumes is through evaporation and condensation mechanisms.[33]

Typically shorter wavelengths give improved mass ablation rate for ns-LA due to reduced plasma screening. However, plasma screening is not expected for fs-LA where the plasma forms at a relatively longer time after the energy deposition at the target surface. Perry *et al.*[34] observed that below 10 ps, ablation threshold in dielectrics varies from the typical $t_p^{1/2}$ dependence (with t_p being the laser pulse duration). Pulse duration in fs-LA is shorter than the electron to ion energy transfer time (τ_{ei}) and heat conduction time (t_{heat}) ($\tau_{ei} \sim t_{heat} \gg t_p$), which are roughly on the order of ~1–10 ps. The energy transport in fs-LA happens in two steps: the photon energy absorption by the electrons and the redistribution of the absorbed energy to the lattice that leads to material removal. Both the wavelengths used in the present study showed near-threshold phenomena, which can be partially explained through the type of ionization and material removal occurring during the fs ablation process.

The physical mechanisms behind ionization and material removal in fs-LA are debated and not well understood.[29] There are two main ionization mechanisms that can happen in fs-LA in the range of laser intensities used in the present study: collisional impact ionization and photoionization. Collisional impact ionization (CII) occurs when free electrons collide with bound electrons, transferring energy, and freeing the bound electrons.[35,36] A series of collisional impacts is known as avalanche ionization, where the number of free electrons increases exponentially.[37] It is reported that[38] at laser intensities $>10^{13}$ W/cm^2, photoionization becomes significantly stronger compared to collisional ionization. Photoionization, sometimes referred to as strong-electric-field ionization, consists of tunnel ionization (TI) and multiphoton ionization (MPI).[36,39,40] Among the photo-ionization mechanisms (MPI and TI), tunnel ionization plays a major role when the laser intensities $>10^{15}$ W/cm^2. The laser intensities used in the present experiment are in the range 10^{13}–10^{14} W/cm^2 and hence MPI is the major mechanism for laser absorption. MPI occurs when multiple photons contribute enough energy to a valence electron to free it from its bond through excitation to metastable quantum states.[41]

The major mechanisms leading to material removal in fs-LA are Coulomb explosion and thermal vaporization. Coulomb explosion occurs when the free electrons form an electron cloud with a strong electric field, which subsequently pulls the ions from the bulk.[42–44] In thermal vaporization, electron collisions increase the temperature at the ablation site above the vaporization temperature, causing ejection of material.[45–47] Coulomb explosion generally occurs for near-ablation threshold energies, whereas thermal vaporization dominates for energies above threshold. Considering the laser intensities used for the present studies (10^{13}–10^{14} W/cm^2), the observed near threshold ICP-MS signal noticed could be caused by Coulomb explosion ablation. At near-threshold, material is closer to being desorbed from the surface than ablated, resulting in fewer particles and only those loosely bound at the surface are being ejected.

For MPI, the difference in ablation threshold energy for the different wavelengths may be due to the difference in the energy of the photon: 3.1 eV for 400 nm wavelength and 1.55 eV for 800 nm. Electrons must absorb more 800 nm photons to be ejected than 400 nm photons. Hence, wavelength also has a role in the near-threshold phenomena, with an increase in threshold energy with increasing wavelength. Previous reports showed that[48] ablation threshold fluences were seen to increase rapidly from λ=267–800 nm and then become almost constant for λ=800–2000 nm for fused silica and CaF_2 crystals, which will exhibit properties similar to the NIST glass standards used here. According to Jia *et al*.,[48] the increase in ablation threshold is thought to be a product of the role of impact ionization (collisional absorption or inverse Bremsstrahlung) and sub-conduction band transitions in the creation of conduction band electrons. According to the Keldysh formula for photoionization rate in solids, photoionization is more effective at lower wavelengths.[49] By extension, this also increases the effectiveness of impact ionization because the more free electrons in the system, the greater the probability of collision.[49] Hence the differences in 400 nm and 800 nm particle counts, LA-ICP-MS signal strength as well as threshold signal phenomena noticed in Figures 2, 4, and 9 may be explained by considering the two-fold photon energy difference between them. 400 nm LA is expected to produce higher mass

ablation rate, which in turn leads to higher ICP-MS signals and decreased detection limits as compared to 800 nm LA at the same fluence.

The improved detection limits for 400 nm at lower energies can be readily understood considering higher particle counts as well as ICP-MS signal levels. According to Figure 4, the ICP-MS signal intensity increases rapidly with increasing laser energy for both wavelengths studied and shows a tendency of saturation especially for shorter wavelengths. Previous studies showed mass loading within the ICP may affect ICP-MS signal levels.[28] The ICP is only capable of ionizing a nominal amount of mass; and once the mass flowing through the ICP exceeds this, the excess particles will not be ionized.[28] Though Figures 2 and 4 indicate that mass loading should be negligible due to the low signal seen, only 8 trace isotopes were detected and the measured isotope signal does not consider the contribution of matrix elements to torch loading, which would contribute considerably to aerosol. However, the particle counts data obtained using CPC (for aerosol containing all particles generated by LA) shows the saturation tendency at higher laser energies and hence the saturation seen in the ICP-MS signal is entirely caused by LA. Another consequence of mass loading is that changes in amount of mass reaching the ICP torch can affect the results seen at the detector, so monodisperse particles (Fig. 11) can yield different elemental ratios than all particle sizes together (Fig. 6). Previous results have shown that higher laser energies produce deeper ablation craters.[50] The generation of deeper craters at higher laser energies may lead to reduced laser-target coupling as well as trapping of the produced aerosol.

Elemental fractionation studies also showed interesting results. U/Th ratio was close to the expected value for both wavelengths studied, both as a function of energy and as a function of particle size. However, the U/Pb results differed from the expected value and were shown to be dependent on the particle diameter. The U/Pb ratio vs. energy gave higher results (~1.2) than the expected ratio (1.083), whereas the U/Pb ratio as a function of particle size gave results that were lower than the expected ratio (~0.8); this can be explained by changes in the aerosol introduced to the ICP-MS. By introducing monodisperse particles, mass loading in the ICP torch is changing, which can affect the ionization capabilities of the torch due to a decrease in introduced aerosol, changing the contribution of torch-induced fractionation effects as compared to polydisperse aerosol. Previous studies have reported fractionation effects via the U/Pb ratio and that corrections are necessary to negate the effects.[51,52] Pb is an extremely volatile element, especially when compared to U, which increases elemental fractionation.[53] It should be noted that during particle formation immediately following ablation, the partitioning between gas and aerosol phase is dependent upon particle size as well as species contained in the vapor phase, which can induce fractionation effects. Agglomeration or aggregation of very small particles can occur, but is not as prevalent in fs-LA as it is in ns-LA.[24] Fractionation also increases with crater formation; the focusing of the laser beam is constantly changing, which changes the apparent fluence coupled to the target.[13,53]

V. CONCLUSIONS

We investigated the role of femtosecond wavelength on particle size distribution, ICP-MS signal intensities, and elemental fractionation in LA-ICP-MS. Our results show that 400 nm

fs-LA yields a higher particle counts and ICP-MS signal than 800 nm LA at the same energy and also has a lower ablation threshold. NIST SRMs (610, 613, 615, and 616) were used to investigate the detection limits at 400 nm and 800 nm fs-LA. Very low detection limits were reached at the saturation point of 400 nm LA, whereas higher energies were necessary to reach the same detection limit using 800 nm wavelength.

The effects of elemental fractionation were also investigated through monitoring the U/Th and U/Pb ratios. The 400 nm results give approximately the same ratio across the entire range of energies, but 800 nm results vary greatly at lowest energies due to ablation threshold effects. Particle size data were obtained to ascertain whether different particle sizes contributed to the elemental fractionation and what effect wavelength had. Results clearly showed that particle size and wavelength have little to no effect on U/Th ratio, whereas particle size has a significant effect on U/Pb ratio.

The present results allow us to conclude that the main differences in 400 nm and 800 nm LA are in the ablation threshold fluence and detection limits as a function of energy. Because of lower ablation threshold for 400 nm, we are able to obtain a higher signal with lower energy. This is specifically due to the ablation mechanism and higher photon energy for 400 nm LA in comparison with 800 nm LA. An extensive study into the specific ablation mechanisms is needed to fully understand the optimum wavelength for fs-LA-ICP-MS.

Finally, it has to be pointed out that three different components of fs-LA-ICP-MS have the capability of contributing to elemental fractionation: laser ablation, particle transport, and ICP-MS (atomization, ionization, and detection). LA is a very complex phenomenon; and in this article, our efforts are directed to understanding the fundamental role that wavelength has on fs-LA-ICP-MS. Hence for this work, ICP-MS operating conditions were optimized before the start of experiments for general operation and steady-state operation was assumed. However, all three components of fs-LA-ICP-MS must be fully investigated and deconvoluted to understand the effect that each can have on fractionation.

ACKNOWLEDGMENTS

This work was partially supported by U.S. Department of Energy, office of National Nuclear Security Administration under Award No. DE-NA0000463.

The findings and conclusions in this paper are those of the authors and do not necessarily represent the views of the National Institute for Occupational Safety and Health. Mention of product or company name does not constitute endorsement by the Centers for Disease Control and Prevention.

References

1. Thakur, SN.; Singh, JP. Laser-Induced Breakdown Spectroscopy. 1st ed. Amsterdam: Elsevier; 2007.
2. Singh J, Kalghatgi A, Parui J, Krupanidhi S. J. Appl. Phys. 2010; 108:054106.
3. Degl'Innocenti R, Reidt S, Guarino A, Rezzonico D, Poberaj G, Gunter P. J. Appl. Phys. 2006; 100:113121.
4. Koch J, Gunther D. Appl. Spectrosc. 2011; 65:155a. [PubMed: 21513587]
5. Fernandez B, Claverie F, Pecheyran C, Alexis J, Donard OFX. Anal. Chem. 2008; 80:6981. [PubMed: 18714966]
6. Brostoff LB, Gonzalez JJ, Jett P, Russo RE. J. Archaeol. Sci. 2009; 36:461.

7. Selih VS, van Elteren JT. Anal. Bioanal. Chem. 2011; 401:745. [PubMed: 21637930]
8. Russo RE, Mao XL, Liu HC, Gonzalez J, Mao SS. Talanta. 2002; 57:425. [PubMed: 18968642]
9. Freydier R, Candaudap F, Poitrasson F, Arbouet A, Chatel B, Dupre B. J. Anal. At. Spectrom. 2008; 23:702.
10. Jeffries TE, Pearce NJG, Perkins WT, Raith A. Anal. Commun. 1996; 33:35.
11. Garcia CC, Lindner H, Niemax K. J. Anal. At. Spectrom. 2009; 24:14.
12. Beauchemin D. Anal. Chem. 2010; 82:4786. [PubMed: 20491450]
13. Eggins SM, Kinsley LPJ, Shelley JMG. Appl. Surf. Sci. 1998; 127–129:278.
14. Bings NH, Bogaerts A, Broekaert JAC. Anal. Chem. 2010; 82:4653. [PubMed: 20465231]
15. Borisov OV, Mao XL, Russo RE. Spectrochim. Acta Part B. 2000; 55:1693.
16. Campos D, Harilal SS, Hassanein A. J. Appl. Phys. 2010; 108:113305.
17. Crank M, Harilal SS, Hassan SM, Hassanein A. J. Appl. Phys. 2012; 111:033301.
18. Freeman JR, Harilal SS, Verhoff B, Hassanein A, Rice B. Plasma Sources Sci. Technol. 2012; 21:055003.
19. Freeman JR, Harilal SS, Hassanein A, Rice B. Appl. Phys. A. 2013; 110:853.
20. Harilal SS, Sizyuk T, Hassanein A, Campos D, Hough P, Sizyuk V. J. Appl. Phys. 2011; 109:063306.
21. Hussein AE, Diwakar PK, Harilal SS, Hassanein A. J. Appl. Phys. 2013; 113:143305.
22. Hola M, Konecna V, Mikuska P, Kaiser J, Palenikova K, Prusa S, Hanzlikova R, Kanicky V. J. Anal. At. Spectrom. 2008; 23:1341.
23. Gonzalez JJ, Liu CY, Wen SB, Mao XL, Russo RE. Talanta. 2007; 73:567. [PubMed: 19073072]
24. Gonzalez JJ, Liu C, Wen SB, Mao X, Russo RE. Talanta. 2007; 73:577. [PubMed: 19073073]
25. Zhu L, Gamez G, Schmitz TA, Krumeich F, Zenobi R. Anal. Bioanal. Chem. 2010; 396:163. [PubMed: 19582436]
26. Verhoff B, Harilal SS, Hassanein A. J. Appl. Phys. 2012; 111:123304.
27. Jeffries TE, Perkins WT, Pearce NJG. Analyst. 1995; 120:1365.
28. Koch J, Walle M, Pisonero J, Gunther D. J. Anal. At. Spectrom. 2006; 21:932.
29. Jiang L, Tsai HL. in Proceedings of NSF Workshop on Research Needs in Thermal. Aspects of Material Removal. 2003:163.
30. Gonzalez JJ, Fernandez A, Mao XL, Russo RE. Spectrochim Acta Part B. 2004; 59:369.
31. Flagan, RC. Aerosol Measurements: Principles, Applications, and Techniques. Kulkarni, P.; Baron, P.; Willeke, K., editors. New York, NY: John Wiley and Sons; 2011.
32. Stuart BC, Feit MD, Herman S, Rubenchik AM, Shore BW, Perry MD. Phys. Rev. B. 1996; 53:1749.
33. Tillack MS, Blair DW, Harilal SS. Nanotechnology. 2004; 15:390.
34. Perry MD, Stuart BC, Banks PS, Feit MD, Yanovsky VA, Rubenchik M. J. Appl. Phys. 1999; 85:6803.
35. Wong K, Vongehr S, Kresin VV. Phys. Rev. B. 2003; 67:035406.
36. Kaiser A, Rethfeld B, Vicanek M, Simon G. Phys. Rev. B. 2000; 61:11437.
37. Pronko PP, VanRompay PA, Horvath C, Loesel F, Juhasz T, Liu X, Mourou G. Phys. Rev. B. 1998; 58:2387.
38. Guy S, Joubert MF, Jacquier B, Bouazaoui M. Phys. Rev. B. 1993; 47:11001.
39. Ammosov MV, Delone NB, Krainov VP. Zh. Eksp. Teor. Fiz. 1986; 91:2008.
40. Arnold D, Cartier E. Phys. Rev. B. 1992; 46:15102.
41. Liu X, Du D, Mourou G. IEEE J. Quantum Electron. 1997; 33:1706.
42. Wang XW, Xu XF. ASME Trans J. Heat Transfer. 2002; 124:265.
43. Cheng HP, Gillaspy JD. Phys. Rev. B. 1997; 55:2628.
44. Stoian R, Ashkenasi D, Rosenfeld A, Campbell EEB. Phys. Rev. B. 2000; 62:13167.
45. Glezer EN, Siegal Y, Huang L, Mazur E. Phys. Rev. B. 1995; 51:9589.
46. Miotello A, Kelly R. Appl. Phys. A. 1999; 69:S67.

47. Toulemonde M, Dufour C, Meftah A, Paumier E. Nucl. Instrum. Methods Phys. Res. Sec. B. 2000; 166–167:903.
48. Jia TQ, Chen HX, Huang M, Zhao FL, Li XX, Xu SZ, Sun HY, Feng DH, Li CB, Wang XF, Li RX, Xu ZZ, He XK, Kuroda H. Phys. Rev. B. 2006; 73:054105.
49. Olivie G, Giguere D, Vidal F, Ozaki T, Kieffer JC, Nada O, Brunette I. Opt. Express. 2008; 16:4121. [PubMed: 18542509]
50. Ben-Yakar A, Byer RL. J. Appl. Phys. 2004; 96:5316.
51. Horstwood MSA, Foster GL, Parrish RR, Noble SR, Nowell GM. J. Anal. At. Spectrom. 2003; 18:837.
52. Russo RE, Mao XL, Gonzalez JJ, Mao SS. J. Anal. At. Spectrom. 2002; 17:1072.
53. Hirata T, Nesbitt RW. Geochim. Cosmochim. Acta. 1995; 59:2491.

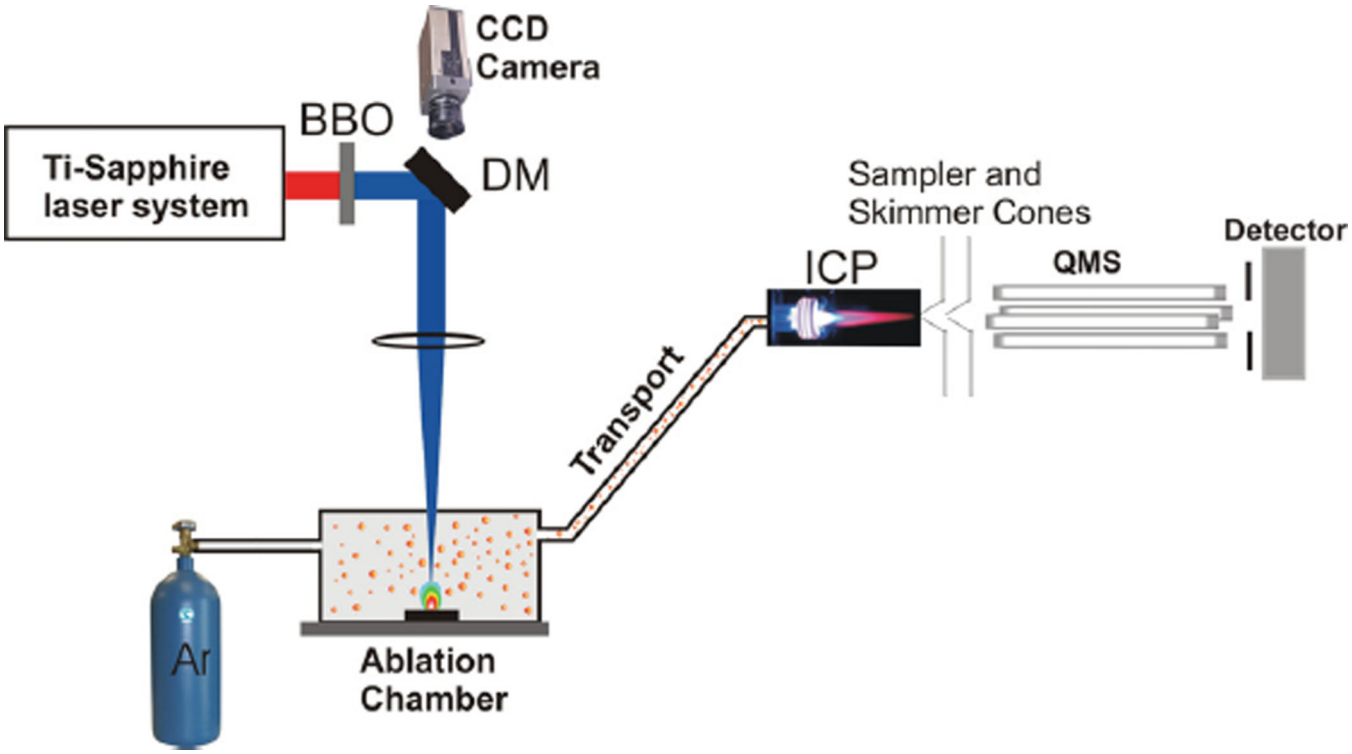

FIG. 1.

Laser system, beam delivery, and analyzer configuration for fs-LA-ICP-MS at 800 nm and 400 nm (components include BBO: beta barium borate crystal, DM: dichroic mirror, CCD: charge-coupled device camera, ICP: inductively coupled plasma, and QMS: quadrupole mass spectrometer). The ablation chamber is mounted on an XYZ translation stage.

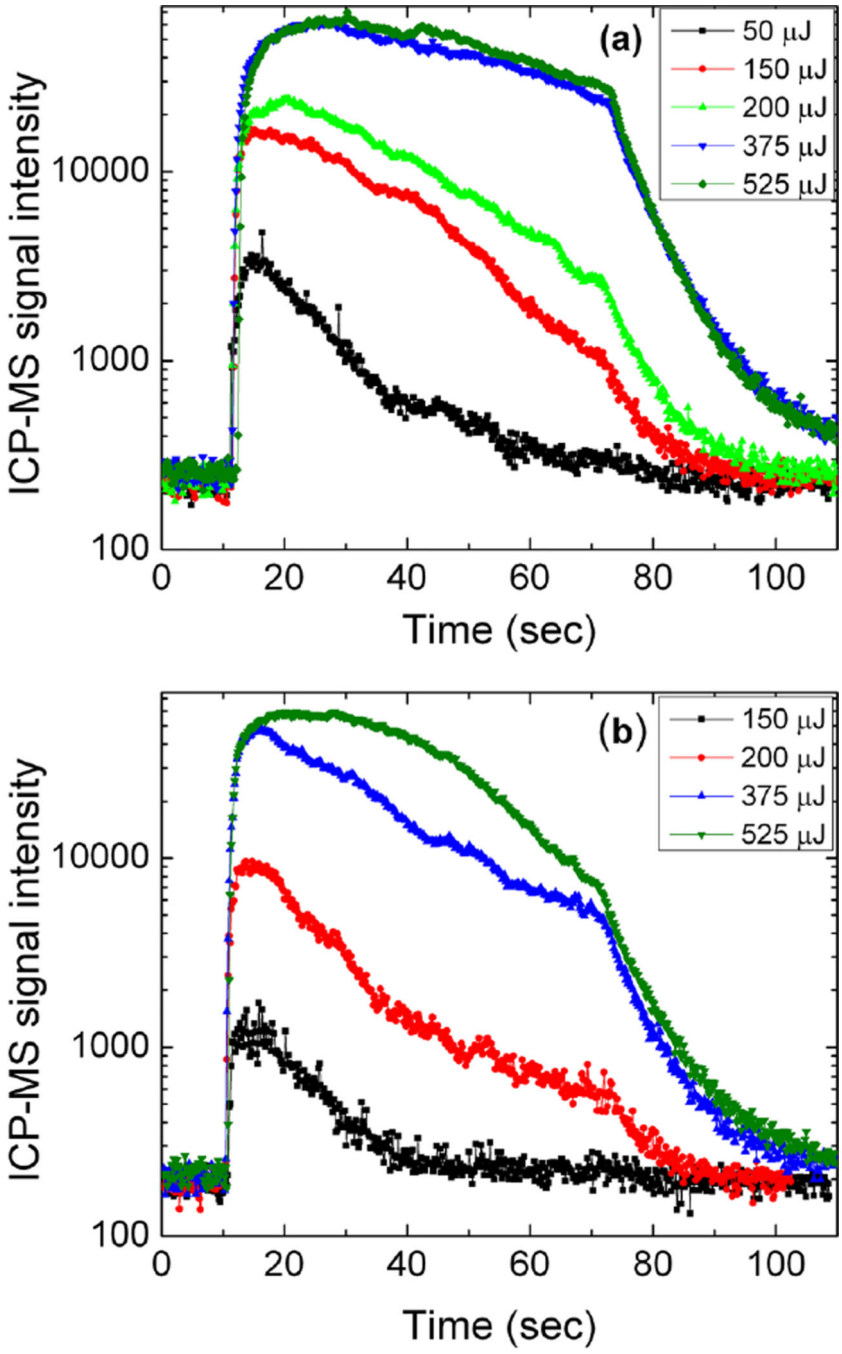

FIG. 2.

ICP-MS signal intensity vs. time at various energies for fs laser ablation of NIST 610 glass standard using (a) 400 nm and (b) 800 nm laser excitation. The laser was triggered at 10 s and fired at a single spot on the target at 10 Hz for 60 s, with 40 s washout time. The lowest energies in both graphs exhibit near ablation threshold characteristics.

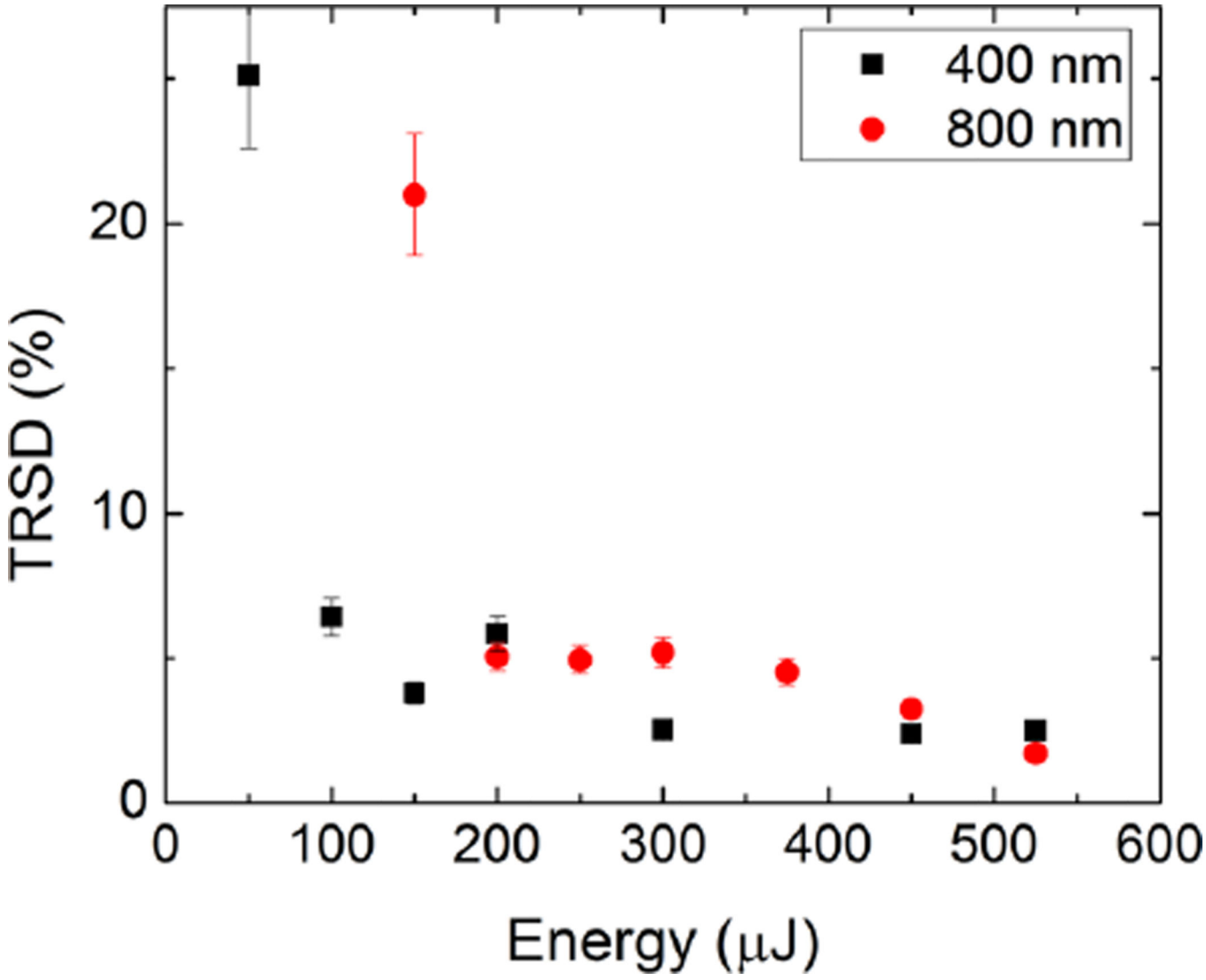

FIG. 3.

Transient RSD as a function of laser energy for all four NIST samples with 400 nm and 800 nm LA. Lower energies show a consistently higher TRSD, and the TRSD is also higher for 800 nm LA than for 400 nm LA, indicating that 400 nm LA is preferable when very precise data are required.

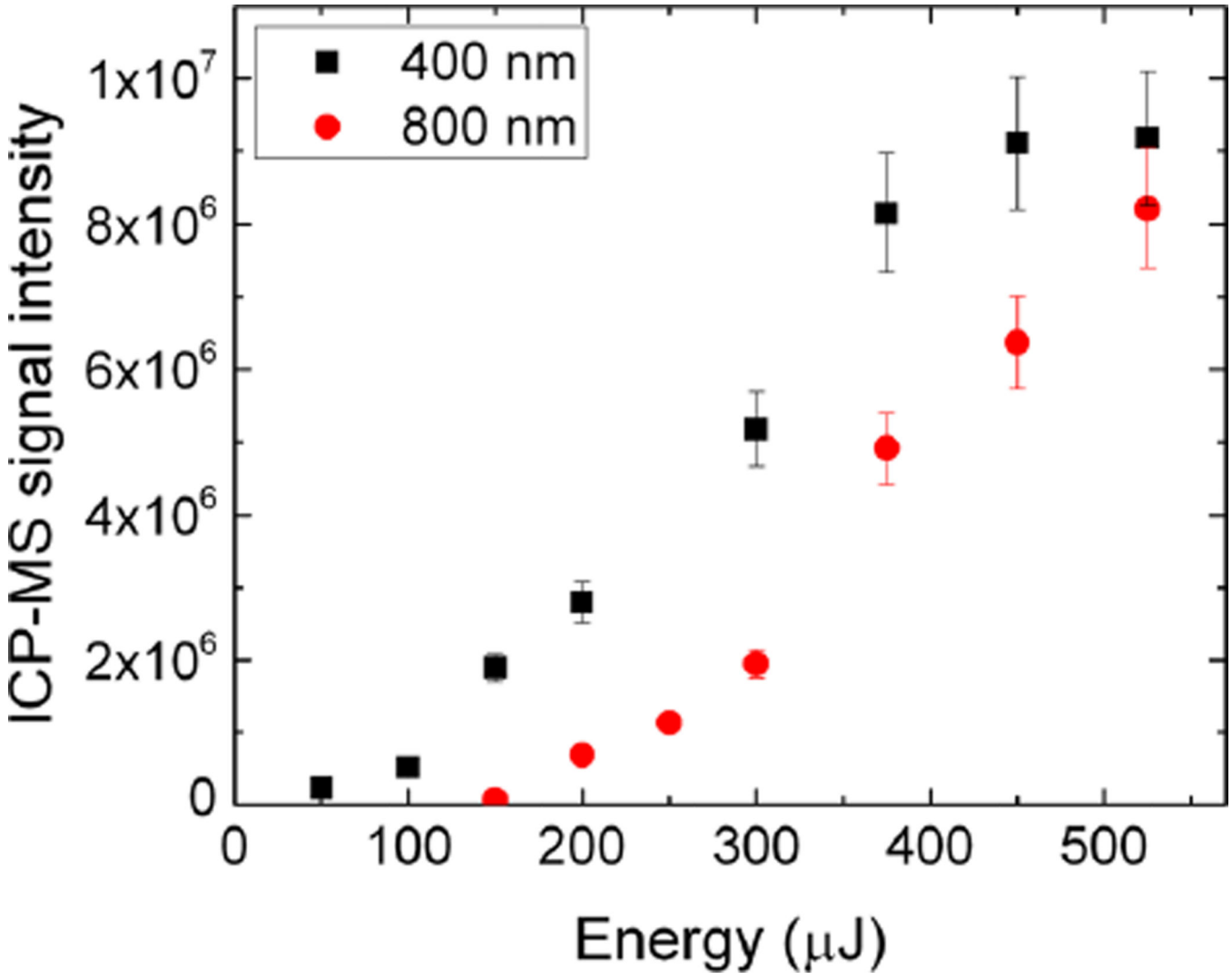

FIG. 4.

Integral ICP-MS signal vs. energy for 400 .nm and 800 nm LA of NIST 610 SRM. The intensity values were computed from 30 s after the signal peaked. The 400 nm signal is higher at all energies but saturates at ~400μJ, whereas the 800 nm signal continues to increase toward the 400 nm saturation level.

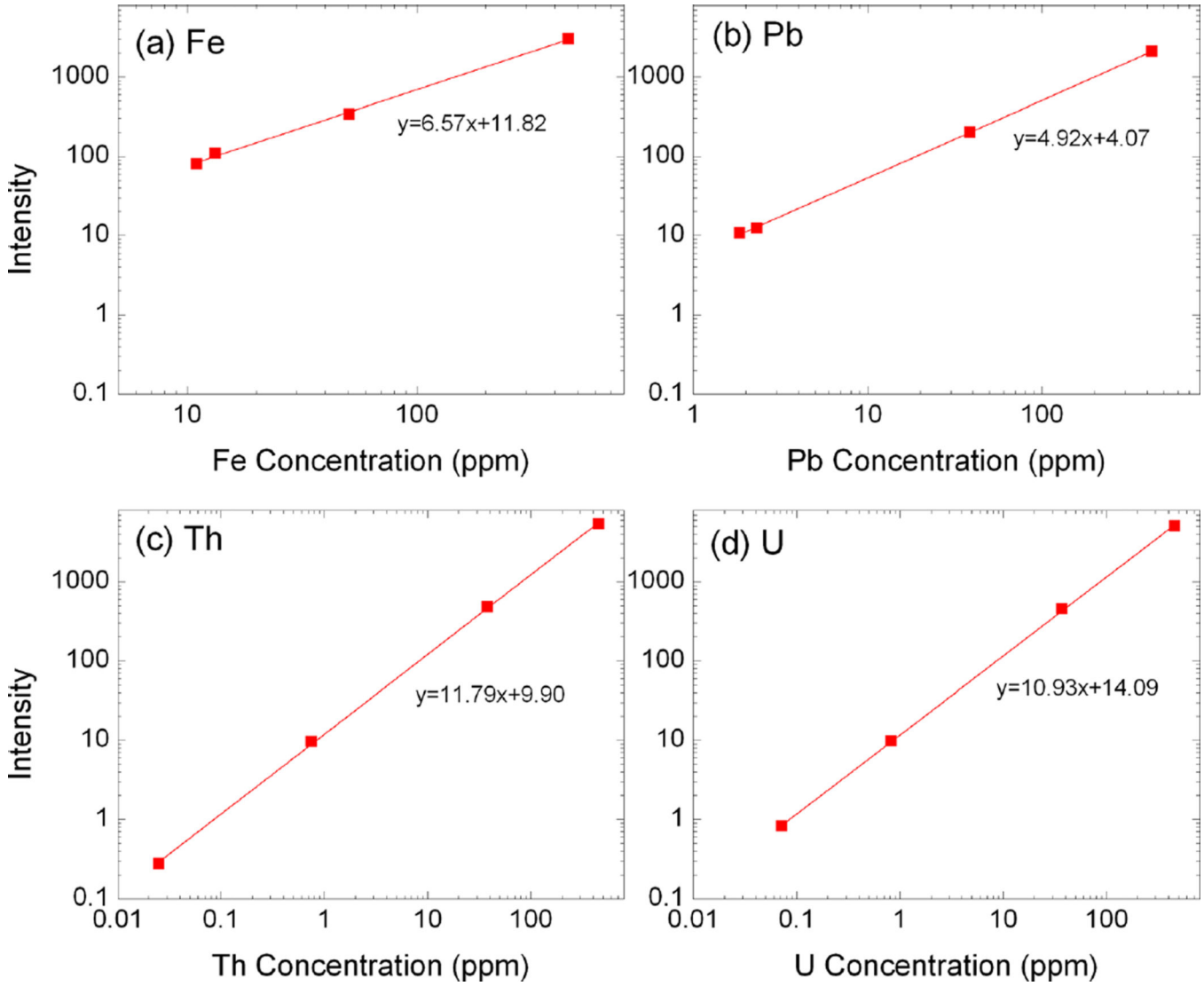

FIG. 5.

Calibration plots for (a) Fe, (b) Pb, (c) Th, and (d) U, for laser ablation at 200 μJ, 400 nm wavelength. Calibration was attained by ablating four NIST glass standards with different concentrations of the selected elements: NIST 610, 613, 615, and 616. The data points were fitted with a linear least squares fit, which was used to determine the detection limit of each element.

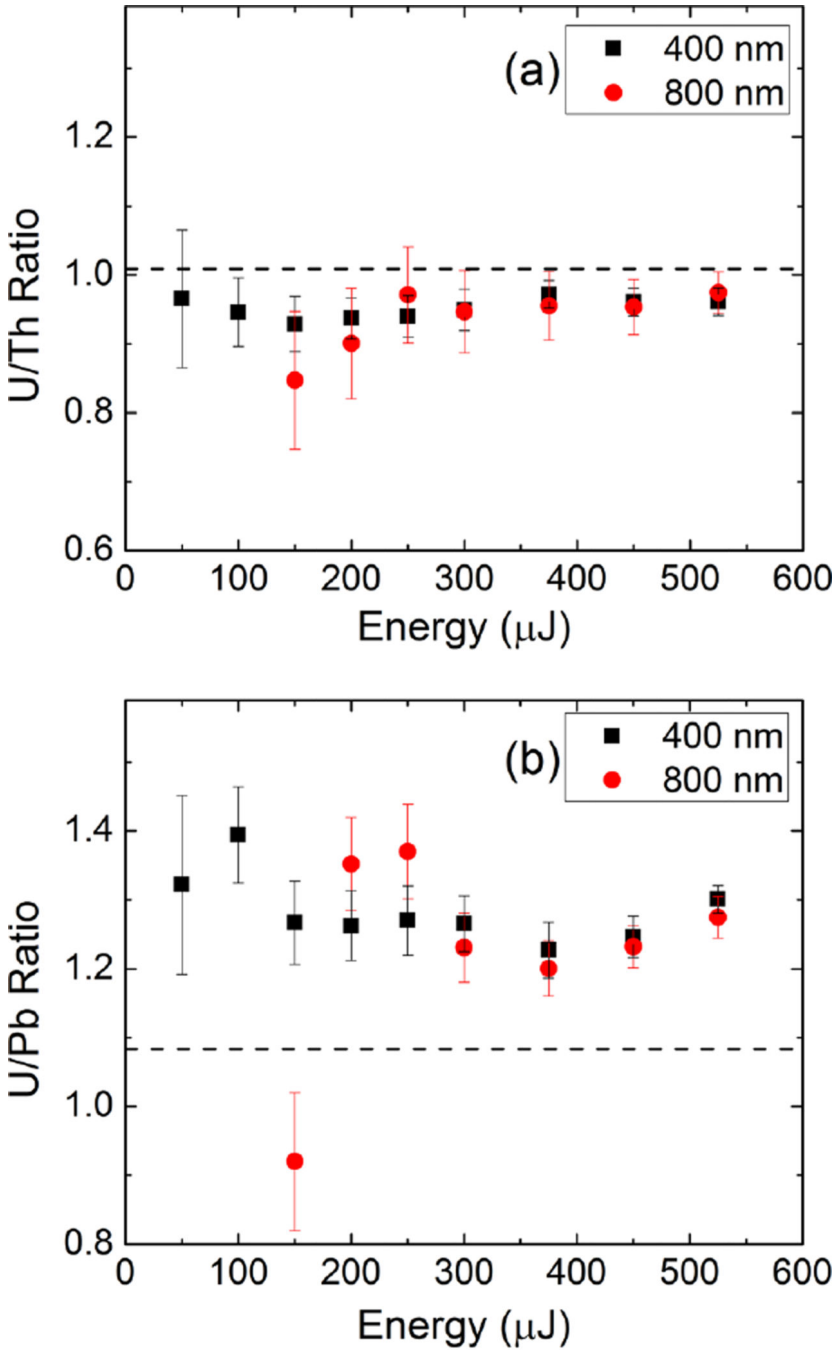

FIG. 6.

Elemental ratios of (a) U/Th and (b) U/Pb are given as a function of energy for 400 nm and 800 nm laser excitations. The sample used for this study was NIST 610. The expected ratios based on elemental concentrations in the standard are 1.009 for U/Th and 1.083 for U/Pb as indicated by the dashed lines; the experimental U/Th ratio is closer to the expected value than the U/Pb ratio. Both ratios are more consistent for 400 nm ablation than 800 nm at lower laser energy levels.

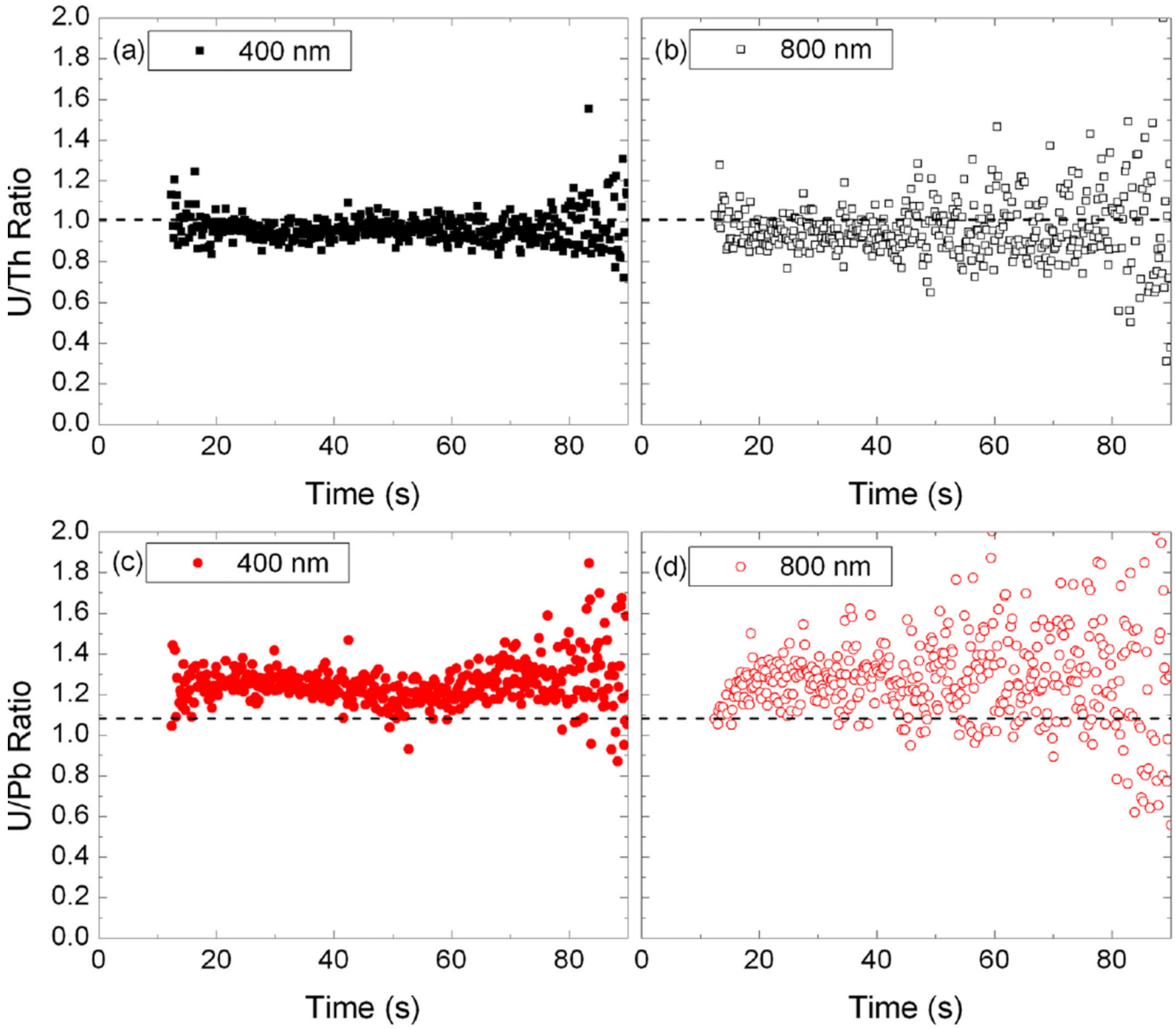

FIG. 7.

Elemental ratios of U/Th at (a) 400 nm and (b) 800 nm, and U/Pb at (c) 400 nm and (d) 800 nm are given as a function of time at 300μJ laser energy. The sample used for this study was NIST SRM 610. The expected ratios based on elemental concentrations in the standard are 1.009 for U/Th and 1.083 for U/Pb as indicated by the dashed lines. Both ratios are more consistent for 400 nm ablation than 800 nm.

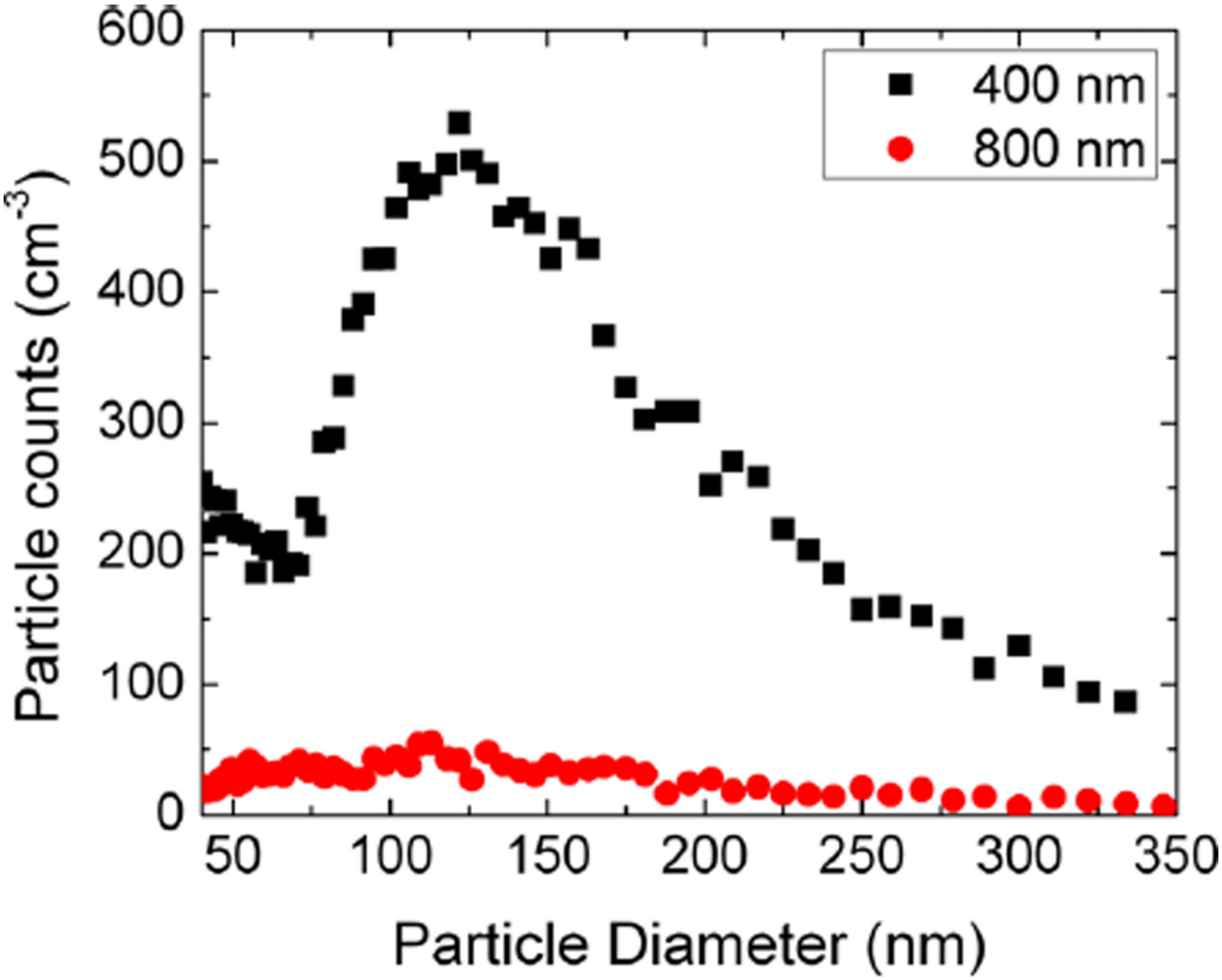

FIG. 8.

Particle counts is plotted as a function of diameter for both wavelengths. For LA, NIST 610 sample was used with laser energy of 300 μJ. The results indicate that the peak particle diameter falls in the range of 100 nm to 150 nm for both wavelengths. Wavelength does not appear to have an effect on peak particle size. However, the particle counts are found to be significantly higher for shorter wavelength.

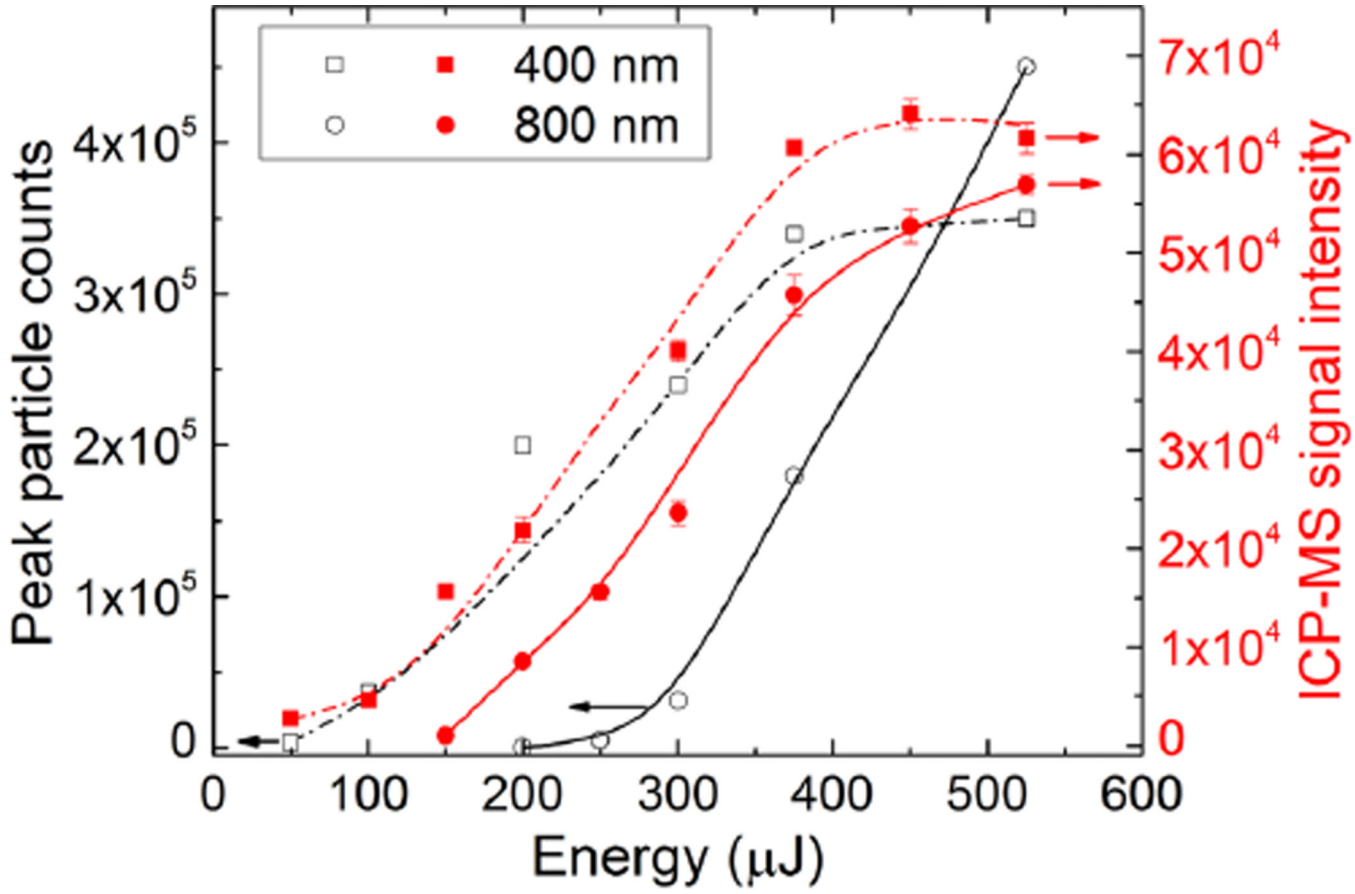

FIG. 9.

Peak number of particle counts obtained for 400 nm and 800 nm laser ablation at various energy levels. ICP-MS signal intensity has been added to the figure for comparison; the open square and circle represent the peak particle counts for 400 nm and 800 nm, respectively, and the filled square and circle correspond to the ICP-MS signal for 400 nm and 800 nm, respectively. The lines here represent the data trend, demonstrating that the peak particle counts follow approximately the same trend as ICP-MS signal.

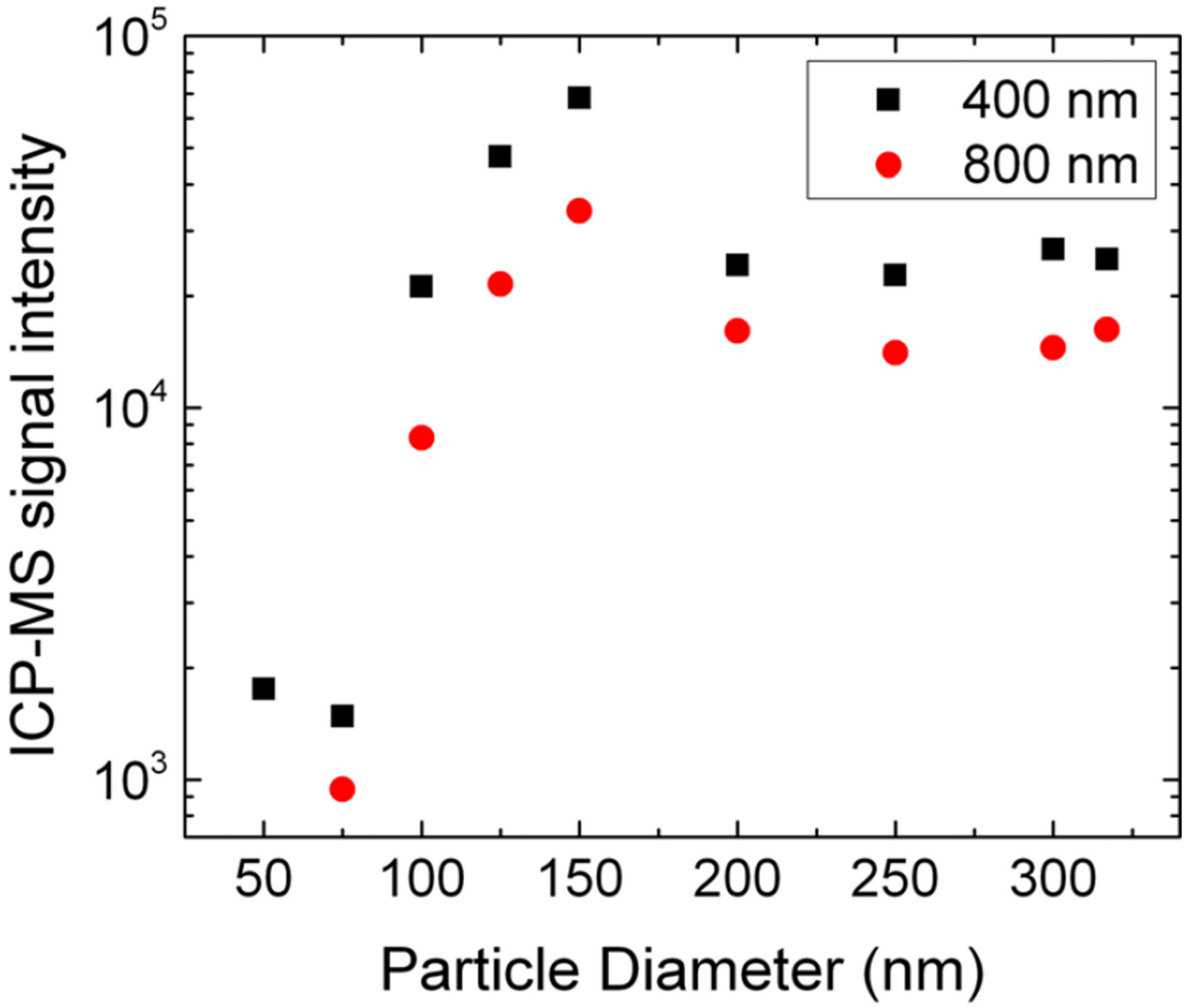

FIG. 10.

ICP-MS signal intensity for various particle diameters for 400 nm and 800 nm LA. For obtaining data, LA was performed on NIST 610 sample with energy of 250 μJ. The maximum signal is seen for 125 nm–150 nm, with steady signal for particle sizes 200 nm–350 nm. The trend is similar for both 400 nm and 800 nm, indicating that the relative contribution of each particle size is not wavelength dependent.

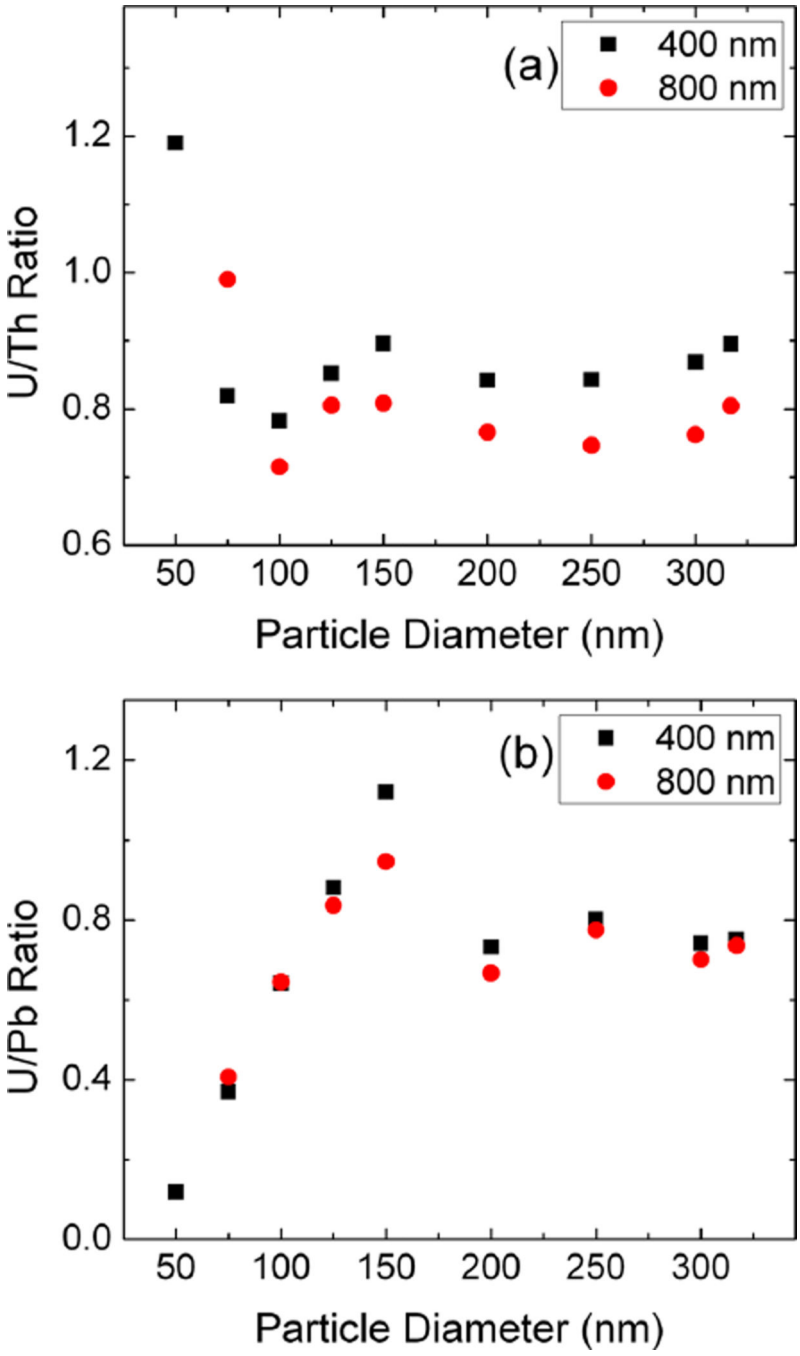

FIG. 11.

To study the role of particle size in elemental fractionation, (a) U/Th ratio and (b) U/Pb ratio vs. particle diameter were obtained for 400 nm and 800 nm LA. NIST 610 was ablated using 250 μJ laser energy. The U/Th ratio data are consistent at all particle diameters. The U/Pb ratio data show that particle diameter plays a major role in the obtained ratio, with the data closest to the expected values for particles with 125–150 nm diameters.

TABLE I

Concentrations (in ppm) of elements analyzed in this study for NIST SRMs 610–616.

Sample	Fe	Cu	Sr	Pb	U	Th
SRM-610	458 ± 9	444 ± 4	515.5 ± 0.5	426 ± 1	461.5 ± 1.1	457.2 ± 1.2
SRM-613	51 ± 2	37.7 ± 0.9	78.4 ± 0.2	38.57 ± 0.2	37.38 ± 0.08	37.79 ± 0.08
SRM-615	13.3 ± 1.0	1.37 ± 0.07	45.8 ± 0.1	2.32 ± 0.04	0.823 ± 0.02	0.748 ± 0.006
SRM-616	11 ± 2	0.80 ± 0.09	41.72 ± 0.05	1.85 ± 0.04	0.0721 ± 0.0013	0.0252 ± 0.0007

TABLE II

Detection limits, given in ppb, at various energies for LA using 400 nm and 800 nm laser wavelengths. Detection limits were computed as three times the standard deviation of the background for each element divided by the slope of the calibration curve. The detection limits are lower at lower energies for 400 nm ablation but at higher energies both 400 nm LA and 800 nm LA approach the same detection limit. Possible error is introduced due to extrapolation of calibration plots to low elemental concentrations.

Energy (μJ)	Iron (ppb)		Lead (ppb)		Thorium (ppb)		Uranium (ppb)	
	400 nm	800 nm	400 nm	800 nm	400 nm	800 nm	400 nm	800 nm
150	7544	144995	614	8460	48	854	104	1978
200	6537	16368	418	1186	34	87	71	188
300	3693	6309	226	381	19	32	39	67
450	2325	2806	139	167	12	14	24	29
525	2528	2593	146	158	12	13	24	27